Oxidation-induced microstructural changes of the TiAl TMN alloy after exposure at 900°C in air

M. C. Galetz[1], A. S. Ulrich[1], C. Oskay[1], D. Fähsing[1], N. Laska[2], U. Schulz[2], M. Schütze[1]

[1]DECHEMA-Forschungsinstitut, High Temperature Materials Group,
Theodor-Heuss-Allee 25, 60486 Frankfurt, Germany
[2]Deutsches Zentrum für Luft- und Raumfahrt (DLR),
Linder Höhe, 51147 Köln, Germany

Abstract

This study focuses on the characterization of oxidation-induced microstructural changes in TNM®-B1 alloy due to the dissolution of oxygen during exposure at 900°C up to 1000h and their correlation with the microstructural subsurface changes as well as its effect on the mechanical properties. For this purpose, the change in the phase distribution is measured during oxidation. In addition to the measurement of the embrittlement during exposure, the fracture strain and nanoindentation hardness of particular phases are assessed to reveal the impact of oxidation and the resulting microstructural changes on their mechanical behavior. The subsurface embrittlement was directly related to the oxygen content as well as significant changes in the phase distribution of the oxygen affected zone. The transformation of β_o-phase into α_2 was proposed as an easily accessible indicator for oxygen uptake depth into the TNM alloy. Finally, the mechanism of embrittlement in the α_2-phase were discussed.

1. Introduction

Titanium aluminides had been in the focus of research for more than three decades before they finally took off as part of modern aircraft engines in 2011 {Bewlay, 2016 MG0092 /id}. Due to their density of about ~4 g.cm^{-3} (half the weight of commonly used nickel-based alloys) they offer a high specific strength and thus a favorable advantage in efficiency, noise reduction and fuel consumption [1,2]. With their properties they also gained interest for application temperatures beyond the present range of ~700 °C. This limit is mainly defined by the strong degradation of their oxidation resistance above that temperature [3,4]. Even third generation alloys such as TNM-alloy with the chemical composition Ti-(24-45)Al-(3-5)Nb-(0.1-2)Mo-(0,1-0,2)B (in at.%) suffer from severe oxidation above this temperature

and oxidize even faster than second generation alloys with a higher Nb-content [5]. Such TMN®-alloys contain the Mo-stabilized bcc β/β_0 phase together with the γ-TiAl and α_2-Ti_3Al phases. β_o is ordered and stable below 1125°C [6] and transforms into β-titanium at high temperatures, which increases high temperature ductility and workability [1,7-9]. On the downside, TNM®-alloys suffer from severe embrittlement of their subsurface zone already after short high temperature exposures [10,11]. Generally oxygen embrittlement is a common feature that the Titanium group metals have in common and is often referred to as "alpha case" [12-14]. The reason lies within the lattice configuration and high oxygen solubility with titanium group metals [15,16]. For titanium aluminides, as early as in 1992, Dowling et al. reported a decrease in room temperature ductility from nearly 2% tensile elongation down to about 0.5% in a Ti-48Al-1V-0.2C alloy after exposure in air at 815°C for 4 h or even in a 10^{-6} Pa vacuum after 100 h at a temperature as low as 775°C [17]. Kelly et al. found similar results, after an oxidation test for as short as 16 h at 649°C [18]. In line with the former cited work, Wu et al. found a subsurface layer strongly enriched in oxygen which developed cracks after exposure at 700°C [19]. As for other Titanium-alloys, this reduced ductility at room temperature can be directly related to oxygen and nitrogen uptake. Accordingly, the loss of ductility can be restored by removal of the surface and subsurface layer following high temperature exposure as shown by several authors [18-22]. One issue related to that is, that the oxygen and nitrogen uptake within the alloy – especially in the different phases - are not easily accessible. Quantified values scatter significantly as shown in Table 1, which denotes the different values determined for the maximum oxygen content in the γ- and α_2-phases. For the β_o-phase, recently a first electron microprobe analysis (EPMA) measurement was reported giving an oxygen maximum in the range of 7-9 at.% [23]. It was found to be in the same order of magnitude of the maximum O-solubility for the beta-phase in the most recent binary Ti-O phase diagram.

Table 1: Overview of the oxygen-content measured in the phases of TiAl-alloys.

Reference	Determination method	Oxygen [at.%]			Oxidation condition and alloy composition
		α_2-Phase	γ-Phase	β_o-Phase	
Ulrich et al. [23]	EPMA	-	-	7-9	900°C, air / TNM-B1
Li et al. (1992) [24]	EPMA	11	3	-	800 – 1100°C / Al_2O_3-Ti diffusion couples
Becker et al. (1992) [25]	EPMA	20	-	-	900 – 950°C, pure oxygen / Ti-35Al-5Nb-0.1C, Ti-36Al (wt.%)
Zhang et al. (1992) [26]	Not specified	12 ± 3	1-2	-	1000 or 1100°C, annealed / estimated from experiments on Ti-16Al-24O, Ti-20Al-30O, Ti-22.4Al-35.1O, Ti-10.4Al-43.1O, Ti-17Al-25O and binary phase diagrams
Gil et al. (1993) [27]	SEM-EDX	20	-	-	900°C, Ar - 20%O_2 / Ti-47Al-2Cr (at%)
Gauer et al. (1994) [28]	EPMA	10-12	-	-	700 – 800°C, air / Ti-25Al-(5-15)Nb (at.%)
Lee and Saunders (1997) [29]	Thermodynamic calculations	13	3	-	1100°C / Ti-Al-O ternary system
Maurice et al. (2007) [30]	XPS	16	2	-	650°C / pure oxygen ($p(O2) = 1 \cdot 10^{-7}$ mbar)

Despite such oxidation issues new TiAl alloys and applications, such as TMB® and TMB®+, aim at even higher application temperatures and enhanced hot workability [7]. This study focuses on the characterization of oxidation-induced microstructural changes in TNM®-B1 alloy due to the dissolution of oxygen and nitrogen during exposure at 900°C and their correlation with the subsurface mechanical properties. For this purpose, the fracture strain and nanoindentation hardness of particular phases are assessed to reveal the impact of oxidation and the resulting microstructural changes on the mechanical behavior.

2. Materials and methods

For this study, a commercial TNM®-B1 alloy with a nominal composition of Ti-43.5Al-4Nb-1Mo-0.1B at% was used. The material was delivered as ingots manufactured by vacuum arc remelting and hot-isostatic pressing (HIP) by GfE, Germany. The TNM®-B1 ingot was cut via arc cutting into 4-point bending test bars (80 x 6 x 4 mm^3) as well as coupon samples (20 x 4 x 6 mm^3) for the other tests described in the following. Before exposure, all samples were ground down to 800-grit (4-point bending test samples) or 1200-grit (oxidation test) and ultrasonically cleaned with acetone for 10 min.

Isothermal oxidation

As received 4-point bending test and coupon samples were isothermally exposed to laboratory air at 900°C in a box furnace for selected durations of 100, 500 or 1000 h. The samples were rapidly heated by placing them into the hot furnace, where they were slowly cooled down to room temperature after the isothermal exposure, by turning off the furnace. The exact cooling curve has not been measured.

4-Point bending test

In the as received state and after exposure 4-point bending tests were conducted at RT employing a universal testing machine (Hegewald & Peschke, Nossen, Germany). The distance between the loading and supporting spans were 36 mm and 64 mm respectively. At least three samples were measured for each condition. Prior to testing, oxidation affected zones were physically removed from three surfaces of the samples, leaving only the one surface affected, which was tested under tensile loading conditions. Loading was conducted using a 33 µm/min constant displacement rate, whereas the samples were unloaded at a constant rate of 100 µm/min. The maximum outer fiber displacement was selected as 1.25 mm, which approximately corresponds to 0.8 % maximum outer fiber strain. This was sufficient to initiate brittle fracture of both the exposed and the as-received specimens. Load-displacement curves were recorded during the test by using a wire extensometer and the stress-strain curves based on the outer fiber strain on the surface were calculated.

Nanoindentation

Nanoindentation measurements were conducted to investigate the hardness of the oxidation affected zone. The maximum indentation depth of 240 nm was kept constant for all measurements, which enabled the characterization of the normal load required to result in the selected indentation depth. At least 8 measurements were taken on average in order to determine the mean normal load for each investigated phase. In order to prevent interaction between the plastic impact zones of different indents, a minimum distance of 10 µm between neighboring indents was employed. The indentation matrix was thereafter correleted with the existing phases by scanning electron microscopy (SEM)-analysis of the different spots.

Microstructural characterization

After oxidation and 4-point bending testing, cross-sections of the samples were manufactured using an automated corundum wheel cutter equipped with a circulating water-cooling system followed by galvanic Ni-plating to preserve the oxide scales and hot mounting in epoxy resin. The metallographic preparation included the wet-grinding to 1200-grit and final polishing with diamond suspensions of 3 and 1 µm respectively. Microstructural characterization as well as measurement of coating zone thickness and oxidation products were conducted by light optical microscopy (LEICA). In addition, the elemental distribution of several samples was investigated via EPMA (JEOL JXA-8100) at a 15 kV

acceleration voltage. Back-scattered electron (BSE) micrographs of cross-sections were recorded using SEM (Philips XL40) with emphasis given on the identification of the beta-phase. Phase fraction analysis was undertaken using a MATLAB (MathWorks)-script, which involves the binarization of BSE-images (see Figure 1) with a selected threshold value and the subsequent vertical white pixel count with defined horizontal intervals, similarly as described in [31]. Afterwards, the position of substrate surface is manually defined with respect to the original micrographs. At least five cross-sectional BSE-images, each taken from different positions on one sample, were analyzed with the above-mentioned method, such that a mean β-phase fraction was quantified as a function of the distance from the surface.

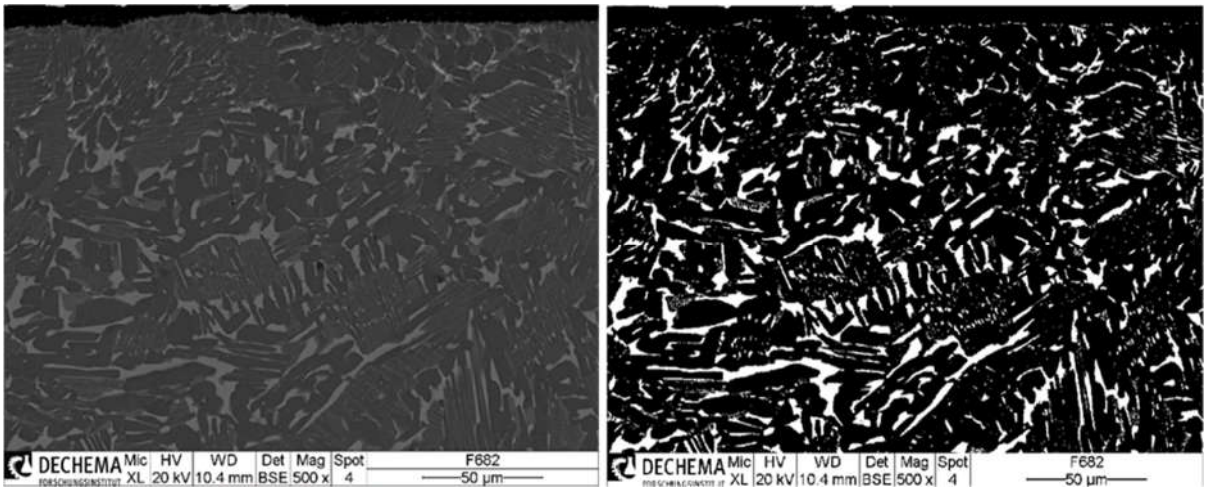

Figure 1: BSE image and corresponding binarized BSE image of the surface area of a TNM-B1 substrate after oxidation for 100 h at 900°C in air. The threshold for binarization is chosen such that the Mo- and Nb-rich β_o-phase can be distinguished (white) from all other phases.

3. Results

Characterization of oxygen (and nitrogen) up-take during oxidation at 900°C

Figure 2 shows the elemental distribution maps acquired by EPMA after exposure at 900°C for 100 h. The surface is covered with a continuous alumina scale. Locally TiO_2 is found on top of the alumina, while underneath a mixed Ti-rich oxide layer which also contains some niobium is present. In addition, niobium is enriched in the metal close to the oxide interface, which corresponds to a Nb depletion zone underneath. Nb in TiAl alloys was shown to enhance the formation of nitrides [32] and indeed, right at the very interface nitrogen is also present in the form of nitrides right underneath the oxide scale, in accordance with literature [33,34]. Beside this, no indication of nitrogen deeper within the material were revealed by EPMA analysis with the limitation of a restricted sensitivity of the investigation method for N. Instead oxygen can be traced down several ten microns deep within the metal. It is quite obvious that oxygen is not equally distributed in the different phases of the material. As shown in Table 1, the

absolute values for oxygen might be subject to a significant divergence, when measured via EPMA spot measurements. However, it is clear that oxygen is enriched in subsurface zone in such areas, which contain a lower extent of Al and Mo, as shown in 2. In Figure 3 the O-signal and Mo-containing zones are superimposed in comparison with the oxygen signal only. This suggests that pronounced oxygen uptake is found in both the α_2-phase (with very little Mo) and the β_o phase, When the oxygen concentration profiles are compared for 100 h and 1000 h exposure as shown in Figure 4a and b, a significant local oxygen uptake could be detected to a depth of about 40 and 110 µm, respectively over a background signal of 3 - 5 at.%. This gives an indication of the thickness of the oxygen affected zone. The strong variations confirm the selective uptake by different phases.

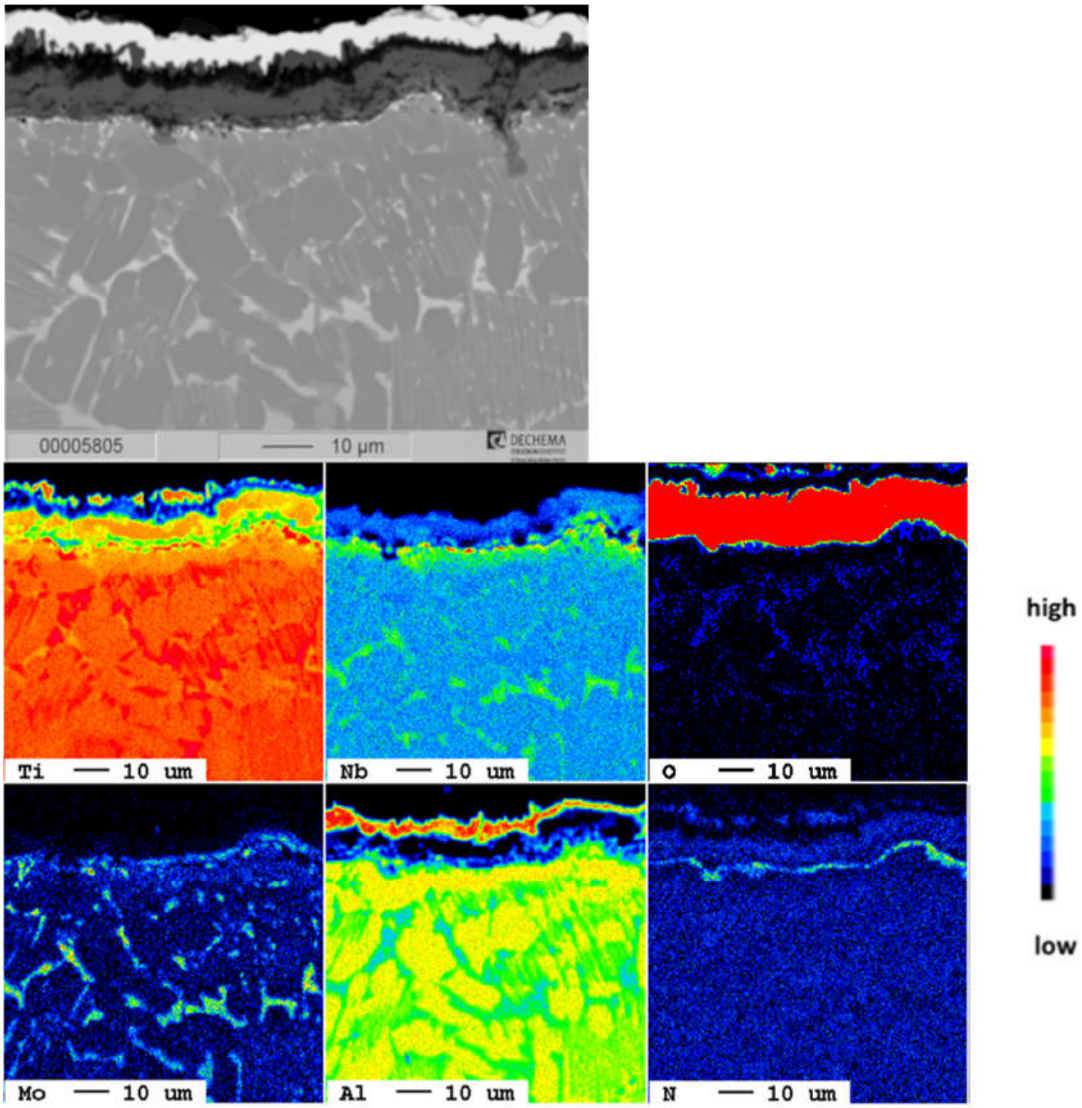

Figure 2: SEM picture and corresponding elemental distribution maps of a TNM-B1 substrate surface after 100 h at 900°C exposure in air.

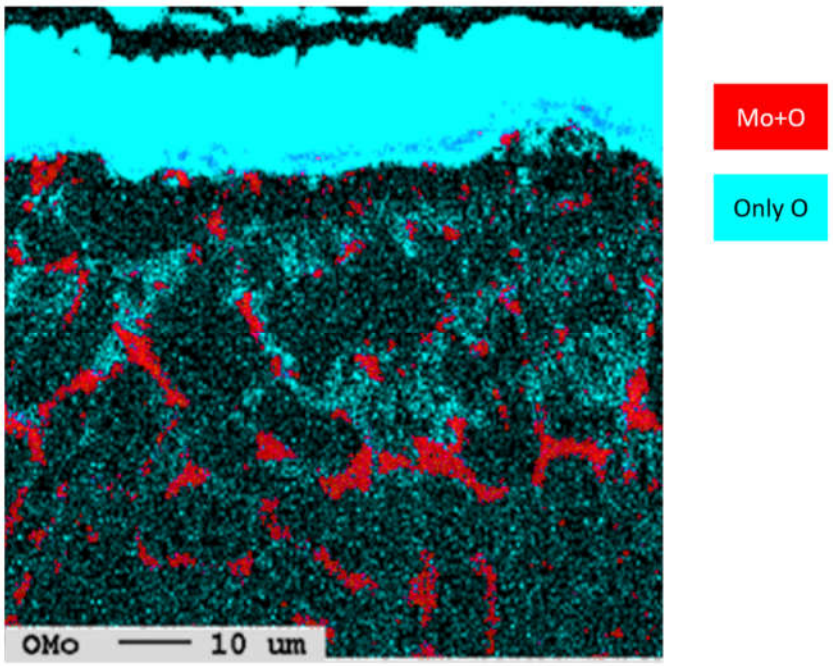

Figure 3: Overlay of EPMA Element Maps. Red indicates the areas in which molybdenum and oxygen are measured. In light blue that locations, where only oxygen is measured.

Beside the oxygen uptake during oxidation, Figure 3 already indicates another feature: a change in the β_o-phase content in the subsurface zone. Figure 4 a and b also shows the mean β_o fraction and oxygen measured as a function of distance from surface for samples exposed to isothermal oxidation at 900°C for 100 (left) and 1000 h (right). From an initial phase fraction of about 13 % in the as-received sample (not shown) only about 3 % is left underneath the oxide scale after oxidation and the depth of the transformation corresponds very well with the depth of the oxygen uptake. It should be noted that both the thickness of the oxygen affected subsurface zone and the β_o-depleted zone increases with exposure duration. Hence it can be postulated that the microstructural changes during exposure specifically the decrease in β_o-phase are driven by the oxygen uptake.

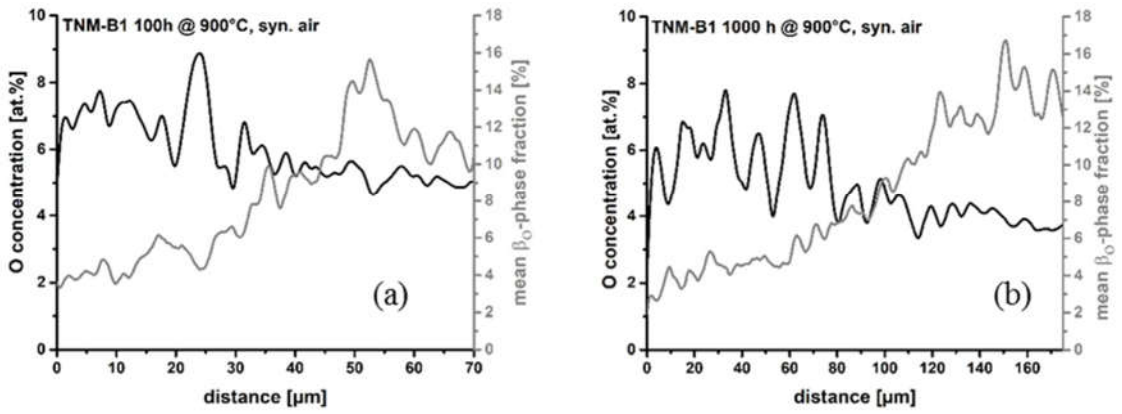

Figure 4: Oxygen concentration (EPMA measurement) and mean β_o-phase fraction (image analysis of BSE-micrographs) as a function of distance from the oxide-metal interface. In a) the analysis is shown for a TNM-

B1 sample after oxidation for 100 h @ 900°C in air while in b) the same is shown after an oxidation time of 1000 h – note the difference in axis scaling.

Change of fracture strain and nanoindentation hardness due to oxidation

Figure 5a illustrates the stress-strain diagrams of the as-received and isothermally oxidized TNM-B1 sample. The as-received TNM-B1 sample showed slight plastic deformation before fracture. On the other hand, oxidation resulted in a linear-elastic behavior without any plastic deformation as well as in a significant reduction in the fracture strain. The fracture strain decreased from 0.7 % in the as-received condition to 0.26 % after 1000 h at 900°C, as shown in 5b. Correspondingly the fracture stress decreases progressively as the oxidation duration increases. The removal of the oxygen enriched and potentially mechanically affected layer to a depth of 40 µm (see the depth profile in Figure 4a) by polishing resulted in the restoration compared to the pristine mechanical behavior, as illustrated in Figure 5b.

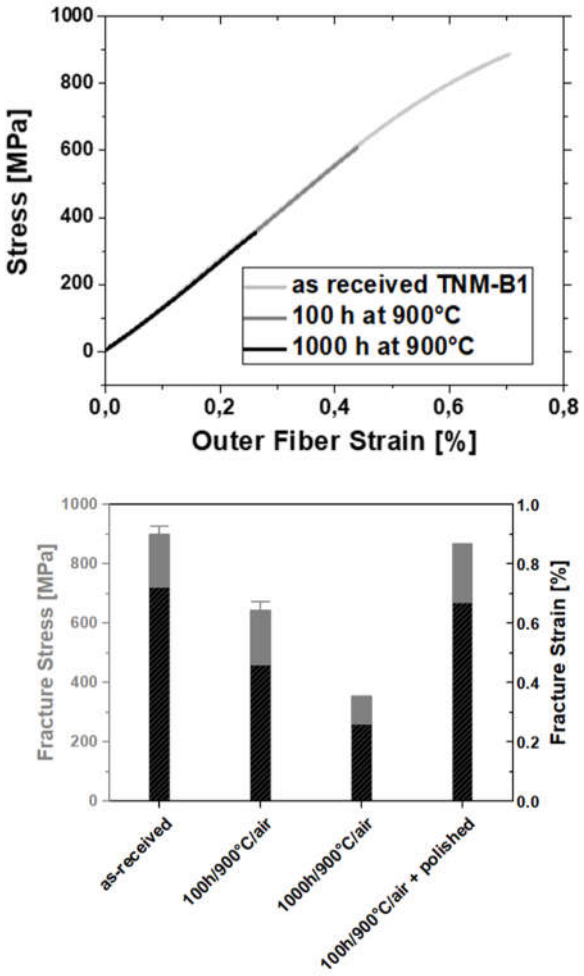

Figure 5: (a) Stress-strain diagrams of as-received and isothermally oxidized TNM-B1 samples; (b) Fracture stress and strain as a function of isothermal exposure duration and the effect of the removal of oxygen-enriched subsurface zone on the fracture stress and strain of TNM-B1 samples.

Cross-sectional nanoindentation was conducted on the oxidized TNM-B1. Despite the observation of an increase in the hardness of the subsurface zone, it is not possible to ascribe this increase to one phase due to the fine-grained lamellar structure.

4. Discussion

While the weight change and oxide scale formation of titanium aluminides has been the topic of numerous studies, in this work the focus lies on the microstructural changes in the subsurface zone and its effect on the mechanical properties. As shown in Figure 4 and 5, the β_o-phase fraction strongly decreases in the subsurface zone during oxidation and the affected depth increases with increasing oxidation time, which is an indicator for a diffusion controlled process. The decrease in β_o-phase fraction can be directly correlated to the depth of increased oxygen concentration. That suggests that by the oxygen uptake the phase equilibrium between γ, α_2 and β_o changes. EPMA analysis reveals that the β_o volume fraction shrinks in favor of the α_2-Ti_3Al phase. Considering the thermodynamical description of the alloy system that phenomenon is unexpected, because up to the eutectoid temperature of T_{eu} = 1115°C, the β_o -phase fraction should increase with temperature as can be seen from the slopes of the solvus lines in the phase diagram in [35], and thus also during an exposure at 900°C. This is in contrast to the observed change in the subsurface zone, where the chemical composition is strongly changed especially by Niobium diffusion towards the surface and Molybdenum partitioning as well as the oxygen enrichment. This composition is not the one of TNM anymore. Considering the chemical changes in the subsurface zone Niobium is enriched underneath the oxide scales. Nb was shown to be beneficial in reducing the weight gain during oxidation while its exact contribution is still under debate. Instead it is unquestionable, that oxygen is diffusing inwards and stabilizes the α_2-phase. It is well known from investigations in the literature, that Nb and Mo are β-phase stabilizing elements [36]. The combination of such different elements can explain the observed phase changes. A schematic of the phase transformation is shown in Figure 6 and might be best evaluated together with the BSE-image in Figure 1.

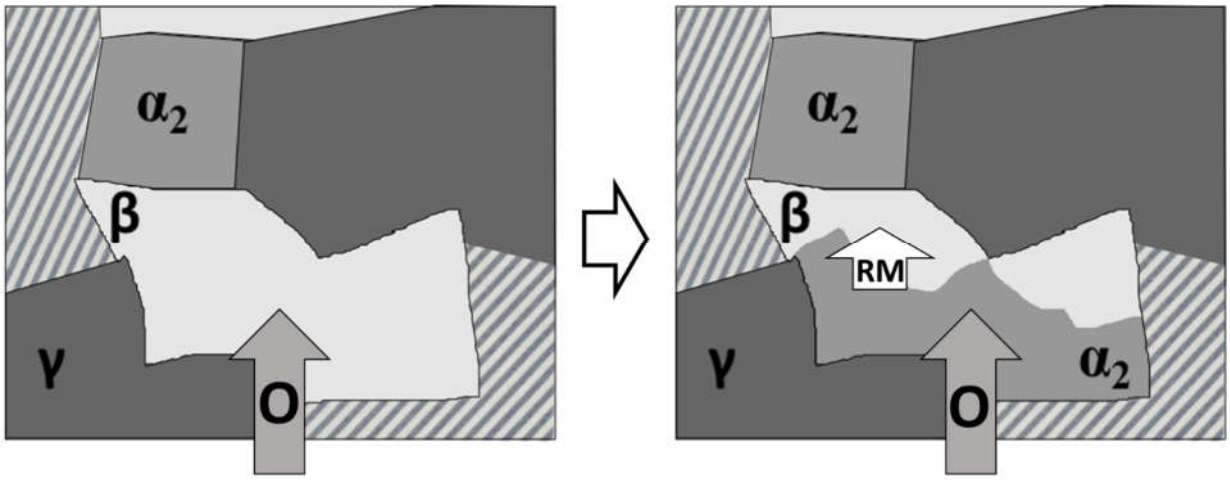

Figure 6: Proposed mechanism for the oxygen-induced phase transformation of β_o-phase to α_2-phase. RM stands for refractory metals.

Table 2: Concentrations of Ti, Al, Nb, and Mo in the β_o-phase over the distance of the phase from the oxide-scale-metal interface of the sample which was oxidized for 100 h at 900°C in lab air. An oxygen concentration of around 8 – 9 at.% comparable to previous work [23] was measured, however, with respect to the measurement method used (EDX) it is neglected in this context. Additionally, the total concentration of refractory metals (RM) is shown.

Depth from surface	Ti [at.%]	Al [at.%]	Nb [at.%]	Mo [at.%]	Total RM
7 µm	46.5	42.0	3.9	7.5	11.4
14 µm	52.1	38.0	4.3	5.5	9.8
55 µm	52.4	37.8	5.9	4.0	9.9
Bulk before oxidation	52.1	38.9	5.6	3.4	9.0

During oxidation oxygen diffuses into the material. As the β_o-phase has a lower oxygen solubility (around half compared to α_2-phase, see table 1), the dissolution of oxygen is lower than in α_2-phase but much higher than in γ. That also means phase transformation from β_o to α_2-phase increases the oxygen solubility of the material, which can contribute to the driving force. This process is in conjunction with the diffusion of the β_o- phase stabilizing elements such as refractory metals which are found in a higher concentration in the β_o- phase in the subsurface region. With increasing oxidation time this process is even more pronounced. For example, a total concentration of refractory metals of 11.4 and 15.6 at.% is found in a surface distance of 7 and 4 µm after an oxidation for 100h and 1000 h at 900°C in lab air, respectively. In the depth it is again slowly reaching the values of the bulk before oxidation [Table 2). It is obvious that the high temperature exposure is rather critical from an embrittlement point of view. The continuous decrease in the stress and strain proves that the mechanical deterioration is directly correlated to the changes in the subsurface zone due to oxidation. On the other hand, it is not perfectly clear if the lower amount of the β_o- phase in the subsurface zone or the oxygen uptake into α_2-phase play the bigger role in the downturn. It is accompanied by higher nanohardness in the subsurface zone before and after exposure to oxygen, however the influence on the hardness alone is rather small. But generally, such oxygen embrittlement is very well known from the α-phase in Ti-, Zr-, and Hf-alloys, when e.g.

metallic titanium absorbs up to 20 at.% oxygen [14,37]. The high solubility for oxygen has been ascribed to the preferential occupation of interstitial Ti_6-lattice vacancies. Such vacancies are completely surrounded by Ti group atoms; when they are occupied by oxygen, it will affect lattice' distortion. For titanium alloys the dissolved oxygen can also induce a beneficial strengthening effect, but the ductility is always decreased. In TiAl alloys Ti_6 -type octahedral sites are present, predominantly within the D19 α_2 -phase structure because the $L1_0$ γ-TiAl structure is composed of alternating planes of Ti and Al atoms in the [001] direction making T_6 vacancy configuration impossible to the subsurface zone this α_2-Ti_3Al phase could also be cubic Z-phase of approximate composition $Ti_5Al_3O_2$ as described in detail in [39]. However, the focus of this work is on the change of the β_o-phase and the potential appearance of z-phase requires TEM resolution is beyond the scope of this study. For the γ-phase oxygen is less critical because $\alpha_{2\ and}$ of the low solubility and due to the fact that slip systems are less affected.

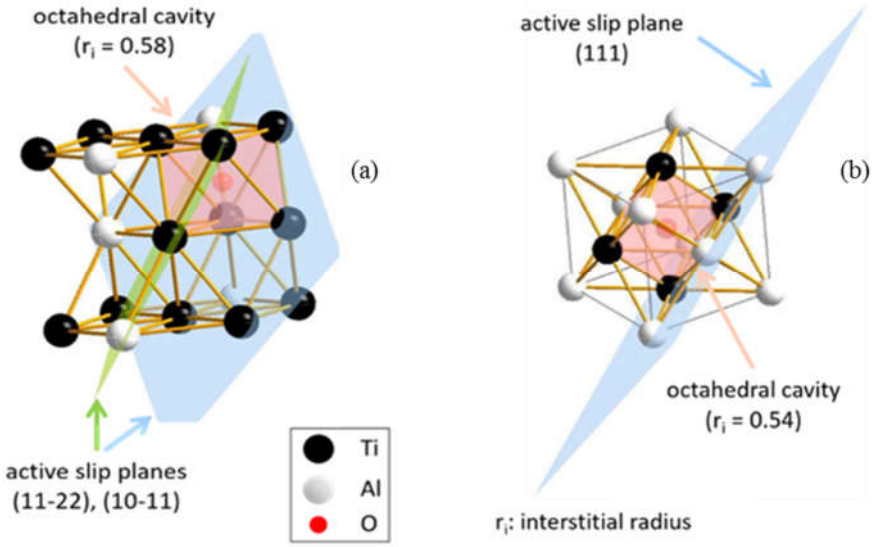

Figure 7: Lattice structures of (a) α_2-Ti_3Al indicating an oxygen vacancy in the close vicinity of the single active slip planes in α_2-Ti_3Al; (b) γ-TiAl indicating the preferred oxygen vacancy, the active slip plane, and the size of the octahedral cavity given in nm.

When the β_o –phase vanishes the only remaining classical dislocation glide can occur in 4 slip systems in γ-TiAl as well as primary by twinning via four mechanical order twins, also in γ-TiAl.

Beside the β_o-phase transformation zone, it will also be interesting to investigate the immediate transition below the oxide. In the case of local Al-depletion in γ-phase before its transformation into α_2, the anti-site defect of Ti on the Al sub-lattice might also provide T_6 vacancies in γ and could even affect oxygen solubility. First SEM EDX measurements showed a much higher oxygen concentration in the γ-TiAl phase directly below the oxide scale and a quite low Ti concentration in a close by α_2 or Z-grain. However, this is beyond the scope of this study, but can be interesting to look at. Nevertheless, the proven high resistance of γ-TiAl phase to oxygen uptake makes this phase an ideal candidate to employ it as a barrier to oxygen e.g. in the form of a coating in [40].

Conclusions

The microstructural changes in the TNM®-B1 alloy due to the dissolution of oxygen and nitrogen during exposure at 900°C in air and their correlation with the subsurface mechanical properties was studied. The following conclusions can be drawn:

i. The subsurface embrittlement is directly related to the oxygen as already proposed in [41].
ii. Oxygen mainly dissolves into the α_2-phase and to a lower extent the β_o-phase, while the γ-phase does not show an increased oxygen content.
iii. Oxygen uptake significantly changes the phase distribution in the affected zone towards a reduced β_o-phase content.
iv. The transformation of the β-phase into α_2 can be used as an easily accessible indicator for oxygen uptake depth into TNM.
v. The strong oxygen uptake in the α_2-phase is related to the T_6-vacancy structure of this phase. The α_2-phase inherently does not exhibit ductile behavior, but the blockage of its only slip system as well as induced internal stresses are suggested explain the increase in hardness and significantly higher embrittlement.
vi. In contrast, the mechanical properties of γ-TiAl with its lower O-solubility are hardly affected by oxygen uptake, which qualifies this phase as a potential barrier.

Acknowledgement

Financial support by the Deutsche Forschungsgemeinschaft DFG under GA 1704/9-2 is gratefully acknowledged. The authors would like to thank Dr. G. Schmidt for performing the ESMA analyses.

304 Reference List

305

306 [1] H. Clemens, S. Mayer, Adv. Engin. Mater. 15 (2013) 191-215.

307 [2] Appel F, Paul JDH, Oehring M. Gamma titanium aluminide alloys: science and technology, John Wiley
308 & Sons; 2011.

309 [3] C. Leyens. Oxidation and Protection of Titanium Alloys and Titanium Aluminides, in: C. Leyens, M.
310 Peters (Eds.). Titanium and Titanium Alloys: Fundamentals and Applications, Weinheim: John Wiley
311 & Sons, Inc.; 2003, p. 187-230.

312 [4] R. Pflumm, S. Friedle, M. Schütze, Intermetallics 56 (2015) 1-14.

313 [5] M. Schütze, S. Friedle. Oxidation Behavior of Intermetallic Titanium Aluminide Alloys, in: I. Baker et
314 al. (Eds.). MRS Symp. Proc., Cambridge University Press; 2013, p. 77-88.

315 [6] E. Schwaighofer, H. Clemens, S. Mayer, J. Lindemann, J. Klose, W. Smarsly, V. Guether,
316 Intermetallics 44 (2014) 128-140.

317 [7] H. Clemens, W. Wallgram, S. Kremmer, V. Güther, A. Otto, A. Bartels, Adv. Engin. Mater. 10 (2008)
318 707-713.

319 [8] H. Clemens, H.F. Chladil, W. Wallgram, G.A. Zickler, R. Gerling, K.-D. Liss, S. Kremmer, V. Güther,
320 W. Smarsly, Intermetallics 16 (2008) 827-833.

321 [9] S. Mayer, P. Ederly, F.D. Fischer, D. Holec, M. Kastenhuber, T. Klein, H. Clemens, Adv. Engin. Mater.
322 19 (2017) 1-27.

323 [10] S. Friedle, N. Laska, R. Braun, M.C. Galetz, H.-E. Zschau, M. Schütze, Corros Sci 92 (2015) 280-286.

324 [11] A. Straubel, S. Friedle, M. Schütze, N. Laska, R. Braun, C. Leyens. Mechanical Properties and
325 Microstructure of a TNM Alloy Protected by the Fluorine Effect and Coated with a Thermal Barrier, in:
326 Y.-W. Kim et al. (Eds.). Gamma Titanium Aluminide Alloys 2014: A Collection of Research on
327 Innovation and Commercialization of Gamma Alloy Technology, 2014, p. 105-109.

328 [12] W.C. Say, Y.Y. Tsai, Surf. Coat. Technol. 176 (2004) 337-343.

329 [13] S.-Y. Sung, Y.-J. Kim, Mater. Sci. Eng. A 405 (2005) 173-177.

330 [14] M.C. Galetz, E.W. Fleischmann, C.H. Konrad, A. Schuetz, U. Glatzel, J Biomed Mater Res B 93B
331 (2010) 244-251.

332 [15] A. Denquin, S. Naka, A. Huguet, A. Menand, Scr. Metall. Mater. 28 (1993) 1131-1136.

333 [16] M. Schütze, Nat. mater. 15 (2016) 823.

334 [17] W.E. Dowling, W.T. Donlon, Scripta Metall Mater 27 (1992) 1663-1668.

335 [18] T.J. Kelly, C.M. Austin, P.J. Fink, J. Schaeffer, Scripta Metall Mater 30 (1994) 1005-1110.

336 [19] X. Wu, A. Huang, D. Hu, M.H. Loretto, Intermetallics 17 (2009) 540-552.

337 [20] S. Draper, B.A. Lerch, I.E. Locci, M. Shazly, V. Prakash, Intermetallics 13 (2005) 1014-1019.

338 [21] S.K. Planck, A.H. Rosenberger, Mater. Sci. Eng. A 325 (2002) 270-280.

339 [22] D.S. Lee, M.A. Stucke, D.M. Dimiduk, Mater. Sci. Eng. A(1995) 824-829.

[23] A.S. Ulrich, N. Laska, A. Straubel, C. Leyens, R. Braun, M.C. Galetz, M. Schütze, Mater High Temp(2017).

[24] X.L. Li, R. Hillel, F. Teyssandier, S.K. Choi, F.J.J. Van Loo, Acta Metall Mater 40 (1992) 3149-3157.

[25] S. Becker, A. Rahmel, M. Schorr, M. Schütze, Oxid. Met. 38 (1992) 425-464.

[26] X. Zhang, C. Hsieh, J. DeKock, Y.A. Chang, Scripta Metall Mater 27 (1992) 1361-1366.

[27] A. Gil, H. Hoven, E. Wallura, W.J. Quadakkers, Corros Sci 34 (1993) 615-630.

[28] L. Gauer, S. Alperine, P. Steinmetz, A. Vassel, Oxid. Met. 42 (1994) 49-74.

[29] B.-J. Lee, N. Saunders, Z. Metallkde. 88 (1997) 152-160.

[30] V. Maurice, G. Despert, S. Zanna, P. Josso, M.-P. Bacos, P. Marcus, Acta Mater. 55 (2007) 3315-3325.

[31] M. Elsaß, M. Frommherz, M. Oechsner, J. Therm. Spray Tech. 27 (2018) 379-390.

[32] N. Zheng, W.J. Quadakkers, A. Gil, H. Nickel, Oxid. Met. 44 (1995) 477-499.

[33] F. Dettenwanger, E. Schumann, M. Rühle, J. Rakowski, H. Meier, Oxid. Met. 50 (1998) 269-307.

[34] A.I.P. Nwobu, H.M. Flower, D.R.F. West. Oxidation of a Near gamma Ti-48.8a/o Al-2.2a/oV Alloy, in: S.B. Newcomb, M. J. Bennett (Eds.). Proceedings of the Second International Conference on the Microscopy of Oxidation Held at Selwyn College, Cambridge, 29-31 March 1993, 1993, p. 357-366.

[35] E. Schwaighofer, M. Schloffer, T. Schmoelzer, S. Mayer, J. Lindemann, V. Guether, J. Klose, H. Clemens, Praktische Metallographie 49 (2012) 124-137.

[36] H. Clemens, M. Schloffer, E. Schwaighofer, R. Werner, A. Geitzenauer, B. Rashkova, R. Pippan, S. Mayer. Advanced beta-solidiying titanium aluminides - Development status and perspectives, in: I. Baker et al. (Eds.). MRS Symp.Proc. 1516, Cambridge University Press; 2013, p. 3-16.

[37] R.W. Evans, R.J. Hull, B. Wilshire, J. Mater. Process. Technol. 36 (1996) 492-501.

[38] A. Menand, A. Huguet, A. Nérac-Partaix, Acta Mater. 44 (1996) 4729-4737.

[39] N. Zheng, W. Fischer, H. Grübmeier, V. Shemet, W.J. Quadakkers, Scripta Metall Mater 33 (1995) 47-53.

[40] J. Grüters, M.C. Galetz, Intermetallics 60 (2015) 19-27.

[41] S.L. Draper, B.A. Lerch, I.E. Locci, M. Shazly, V. Prakash, Intermetallics 13 (2005) 1014-1019.